Compliance criteria for power oscillation damping functions in power electronic interfaced resources

Pierre Demey, Junior-Le-Roy Noupowo Kenne, Carmen Cardozo, Adrien Guironnet, Gilles Torresan, Sami Tliba

To cite this version:

Pierre Demey, Junior-Le-Roy Noupowo Kenne, Carmen Cardozo, Adrien Guironnet, Gilles Torresan, et al.. Compliance criteria for power oscillation damping functions in power electronic interfaced resources. 23rd Wind & Solar Integration Workshop, energynautics, Oct 2024, Helsinki, Finland. hal-04851379

HAL Id: hal-04851379
https://hal.science/hal-04851379v1

Submitted on 20 Dec 2024

23^{rd} Wind & Solar Integration Workshop | Helsinki, Finland | 08 –11 October 2024

COMPLIANCE CRITERIA FOR POWER OSCILLATION DAMPING FUNCTIONS IN POWER ELECTRONIC INTERFACED RESOURCES

Pierre Demey[1], Junior Noupowo[2], Carmen Cardozo[1]*, Adrien Guironnet[1], Gilles Torresan[1], Sami Tliba[2]

[1]*Réseau de Transport d'Electricité, 7C Place du Dôme, Immeuble Window, Puteaux, France*
[2]*Laboratoire des Signaux et Systèmes, Université Paris-Saclay–CNRS–CentraleSupélec, 3, Rue Joliot-Curie, Gif-sur-Yvette, France*
**carmen.cardozo@rte-france.com*

Keywords: POWER OSCILLATION DAMPING, POWER PARK MODULE, SMALL SIGNAL STABILITY

Abstract

This paper examines the limits and opportunities of various approaches for specifying and designing power oscillation damping (POD) controllers for power electronic interfaced resources (PEIR) to improve inter-area mode damping.While frequency-domain requirements are increasingly recognized as essential for ensuring stability and robustness across a specified frequency range, further efforts are needed to achieve consensus among industry stakeholders regarding suitable compliance criteria and verification methods. At the same time, simulation benchmarks tailored to capture relevant dynamics have proven effective in assessing time-domain performance. Through controllability and observability analysis, the study highlights the significant dependence of the device under test's (DUT) closed-loop response on the specific settings of the test system.

1 Introduction

Historically, the small-signal stability (SSS) of power systems dominated by synchronous generators (SGs) has relied on power system stabilisers (PSSs) installed in large power plants. PSSs primarily act on automatic voltage regulators (AVRs) to enhance the damping of low-frequency oscillatory modes inherent to individual units (typically below 2 Hz), known as local modes. Hence, in addition to traditional steady-state output, limited overshoot, and specific response times, AVR performance requirements may include damping constraints.

Additionally, PSSs are expected to contribute to the damping of inter-area modes, which involve multiple units in large interconnected systems. Defining exhaustive technical specifications and suitable compliance verification procedures to assess this performance is today an active research field [1, 2].

In France, RTE traditionally imposes *robustness* requirements on AVRs to address modelling approximations during control design and the ever-evolving nature of the grid. To secure grid access, large power plants must demonstrate sufficient *stability margins* with respect to some physical parameters. Specifically, in addition to settling within a 5% band of the reference in less than 10 seconds and meeting steady-state error limits, stability margin thresholds are also enforced [3] (see Appendix A for definitions and interpretation):

- Modulus margin $M_m \geq 0.34$,
- Complementary modulus margin $M_{mc} \geq 0.33$,
- Delay margin $\Delta\tau \geq 34$ ms.

Recent work has focused on refining this requirement to better account for inter-area modes, suggesting the introduction of a limit on the maximum phase shift between the torque generated by the PSS and the SG speed. In particular, the product of the generator and PSS transfer functions could be required to stay within a safety phase margin, typically $\pm 30°$, over a defined frequency range. Compliance with this requirement should be demonstrated through both time-domain simulations of step responses and frequency-domain characteristics, such as Bode or Nyquist diagrams, for specific transfer functions. Additionally, bounds on the controller gain and the ratio between the gains of specific transfer functions may also apply to ensure adequate stability margins [4, 5].

Power electronic interfaced resources (PEIR) have the capability to modulate injected active or reactive power within a specific frequency range by incorporating dedicated control loops, commonly referred to as power oscillation damping (POD) controllers in the context of HVDC applications. Notably, in Europe, transmission system operators (TSOs) have shown increasing interest in POD functions over the past decade to enhance the damping of inter-area modes [6] and mitigate the risk of oscillatory events [7, 8].

The capability of Power Park Modules (PPM) to provide this functionality has been discussed in the literature [9], and it can be mandated as grid connection requirement in accordance with European Connection Network Codes (CNC) [10]. However, a key challenge remains the proper formulation of the requirement, compliance criteria, and verification benchmarks to guide manufacturers in developing robust solutions that effectively provide positive damping to the system [11].

This work aims to provide a TSO's perspective on this issue by exploring the use of a two-area benchmark, tailored to replicate inter-area modes, in the POD control design. While PSSs were developed to primarily damp local modes, simple Thevenin equivalents sufficed for system representation. However, as the expectation for contribution to the damping of inter-area modes grew, the *need* for more detailed grid models capable of capturing the relevant dynamics emerged. However, creating accurate AC grid equivalents for stability assessment remains challenging, as the dynamics of large-scale power systems are dominated by the interaction of thousands of subsystems with uncertain models. Moreover, its properties continuously evolve with fluctuating loads and the regular connection or disconnection of assets (e.g. generating units).

To address this challenge, control design solutions that rely on minimal information—typically focusing exclusively on mode frequency, which remains relatively constant for inter-area modes—have garnered significant attention. This principle could also be naturally applied to POD functions.

In practice, control design falls within the scope of the manufacturers, while system owners must prescribe requirements rather than dictate specific techniques. Consequently, attention has shifted towards formulating *damping requirements*, and with these requirements comes the need for clearly defined compliance criteria and verification procedure.

In this context, developing suitable testing benchmarks to assess performance has proven invaluable for enhancing communication and understanding among various stakeholders, especially when detailed dynamic models are often encrypted to protect intellectual property. Nonetheless, careful consideration must be given to the guarantees such approaches provide when addressing SSS phenomena.

Section 2 establishes the modelling framework based on system state-space representations of several variants of the considered benchmark, which are automatically derived from a phasor-domain nonlinear simulation tool (see Appendix B for details). Section 3 presents a frequency-domain analysis to evaluate the modal degrees of controllability and observability of the considered transfer function. Section 4 proposes a POD design based on stability margins, following an approach similar to the one typically used for PSS design in France to comply with RTE requirements. Section 5 evaluates the resulting performance through time-domain simulations, while conclusions are drawn in Section 6.

2 Benchmark, scenarios and POD structures

Section 2.1 describes the considered simplified benchmark, while Section 2.2 outlines the scenarios under examination and Section 2.3 presents the POD schemes used in this study.

2.1 Two-IG test benchmark

By connecting two low-order system frequency response models [12], referred to hereafter as inertial grids (IGs), through a transmission line (see Fig. 1), it is possible to create a test system with a settable dominant mode.

The frequency and damping of this mode depend on the connection impedance, Z_{eq}, and the inertia constants, H_i, of the IGs. Following linearisation around a given operating point and neglecting system resistance, the inter-area mode frequency, f_{IA} can be approximated by Eq. (1) [13, 14]:

$$f_{IA} = \frac{1}{2\pi}\sqrt{\frac{U_{1,0}U_{2,0}\omega_0 cos(\delta_0)}{2H_{eq}X_{eq}}}, \tag{1}$$

where ω_0 is the nominal frequency, H_{eq} is the equivalent inertia constant, $U_{1,0}$ and $U_{2,0}$ are the magnitude of the voltage sources associated to the two IGs, and δ_0 is the angle difference between these two sources obtained from a power flow (PF) solution. For selected parameters, which are based on [2] and provided in Appendix C, the mode frequency is 0.42 Hz.

2.2 Scenarios under investigation

The system's initial operating points are defined by specifying the active and reactive power injected by the device under test (DUT) at the point of common coupling (PCC) and by IG 2 at PCC E. The voltage is imposed at the terminals of IG 1.

- IG 1: $U_{1,0} = 1.072$ pu, $\theta_{1,0} = 0°$ (slack bus in PF),
- IG 2: $P_{2,0} =$ -100 MW, $Q_{2,0} = 0$ Mvar (consuming power),
- DUT: $P_{3,0} = 50$ MW, $Q_{3,0} = 0$ Mvar (injecting power).

Then, as illustrated in Fig. 1, different scenarios can be defined by varying the impedance values of lines L1 and L2, which affects the proximity of the PCC to one of the IGs. The equivalent impedance is kept constant to preserve the properties of the dominant mode. A location parameter (α) is used to define the position of the PCC, such that $X_1 = \alpha X_{tot}$ and $X_2 = (1-\alpha)X_{tot}$ [15]. Five possible connection points are considered, resulting in five different scenarios, with the corresponding PF results provided in Appendix C (L3 = 0 km in all scenarios).

- Case A: $\alpha =0$
- Case B: $\alpha =0.25$
- Case C: $\alpha =0.5$
- Case D: $\alpha =0.75$
- Case E: $\alpha =1$

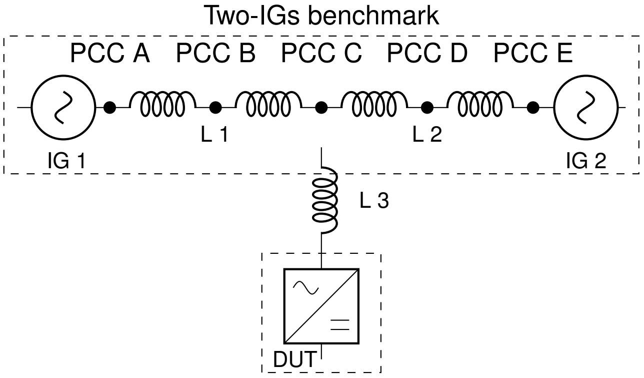

Fig. 1: Schematic representation of the two-IGs benchmark

As illustrated in Fig. 2-left, due to the asymmetry in the sizes of the IGs, the system's centre of inertia (COI), where frequency changes are minimal compared to other positions along the line, is not located midway between the two areas but closer to IG 2 [15]. Specifically, $\alpha_{COI} = 0.766$ [14], meaning that at PCC D, the inter-area mode is not visible in the frequency signal. Fig. 2-right shows the voltage at PCC B, C, and D for the same event—a 25 MW active power load variation at PCC A—illustrating that oscillation information is also captured in the voltage signal along the line, with higher amplitude near IG 1 and lower amplitude at PCC D.

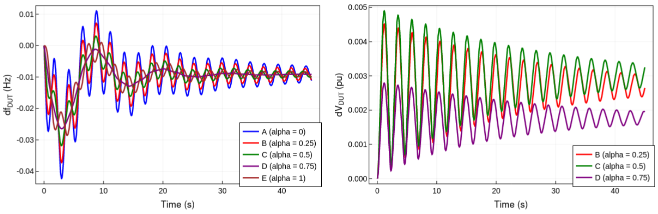

Fig. 2: Active power variation (25 MW) at PCC A: Frequency (left) and voltage (right) at different locations (PCC A-E)

Additionally, Fig. 3 shows the frequency difference between the two IGs, $\Delta f = f_1 - f_2$ (in pu), for a 5 MW active and 5 Mvar reactive power reduction in the DUT, considering different locations (PCC A-E). Since the IGs are modeled as fixed voltage sources with variable frequency, reactive power load variations at nodes PCC A and E do not cause any system disturbance. The poorly damped (1.6%) inter-area mode is excited in all three cases.

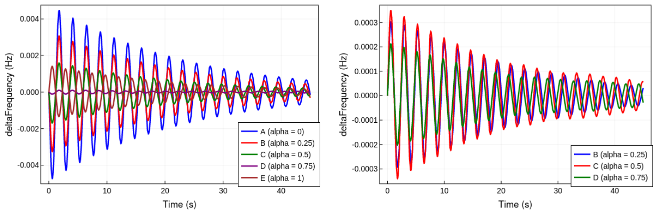

Fig. 3: Frequency difference between both inertial grids following an active and a reactive power variation by the DUT at PCC A, B, C, D and E

By analogy to PSS design, PODs are developed to exploit the relationship between inter-area modes with DUT active and reactive power modulation, aiming to provide positive damping to system oscillations. In the following sections, a theoretical approach is adopted to explore how the choice of controller structure, DUT location, and technical constraints—particularly the available regulating power band—affect the effectiveness and robustness of the solution.

Discussion on energy availability for active power modulation and the specific control modes of the PEIR are beyond the scope of this paper. For simplicity, we consider a battery energy storage system (BESS) operating in a classical grid-following mode with a constant reactive power reference

2.3 *POD SISO structures*

Three possible POD structures based on a single-input-single-output (SISO) scheme are examined. As illustrated in Fig. 4, the input is either the voltage magnitude or frequency, while the output is either the active or reactive power, resulting in:

a)POD-Q(f) (based on frequency measurement)
b)POD-Q(V) (based on voltage magnitude measurement)
c)POD-P(f) (based on frequency measurement)

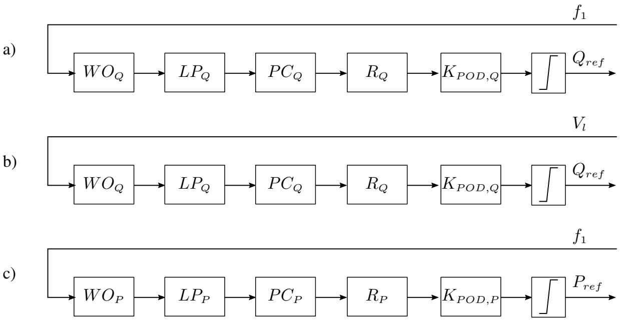

Fig. 4: (a) POD-Q based on f, (b) POD-Q based on V, (c) POD-P based on f.

Each controller consists of the series connection of:

- a proportional gain, K_{POD},
- a washout filter $WO(s) = \dfrac{s\,T_{wo}}{1 + s\,T_{wo}}$,
- a low-pass filter $LP(s) = \dfrac{1}{1 + s\,T_{lp}}$,
- a phase compensator $PC(s) = \dfrac{1 + s\,T_1}{1 + s\,T_2}$, and
- a second-order filter $R(s) = \dfrac{1}{\frac{s^2}{\omega_r{}^2} + \frac{2\xi_r\,s}{\omega_r} + 1}$, possibly resonant.

The parameters' setting depends on the chosen control strategy. Each control strategy can lead the designer to switch off the use of one or several filters involved in the control structure by an adequate choice of parameters. This structure is closely inspired by that in [9], except for the second-order filter, possibly resonant, which has been inserted to offer more possibilities to address the damping of some important modes.

Before proceeding to the POD control designs in Section 4, the next section offers insights into the intrinsic properties of the benchmark, which are essential for understanding and interpreting the obtained results.

3 Controllability and observability assessment

The joint controllability and observability level (JCOL) for a given eigenmode of a linear time-invariant (LTI) system refers to the sensitivity of this mode in the response of a given input-output transfer function of this system. It is derived from the classical modal controllability and observability quantities, as defined for power systems in [16] or [17].

After performing the fraction expansion of the system's transfer function, the JCOL is defined as the modulus of the residue associated with a given mode (pole). The relative JCOL (RJCOL) is defined as the ratio of the mode's JCOL over the direct transmission value, assuming it exists. Otherwise, one uses the JCOL. On the other hand, for non-strictly proper transfer functions (*i.e.* with a non-zero direct feedthrough term), the proximity of a mode's resonance frequency with the closest anti-resonance one in a frequency response allows assessing the JCOL of a mode. The closer an anti-resonance frequency is to a mode's resonance frequency, the more this mode will be uncontrollable and/or unobservable, resulting in a controller being weakly able to modify this mode's dynamic in a closed-loop.

In our case, the frequency responses on Bode's diagram in Fig. 5 show us the most favourable scenario for the POD's design, depending on the chosen control structure among the ones enumerated in Subsection 2.3.

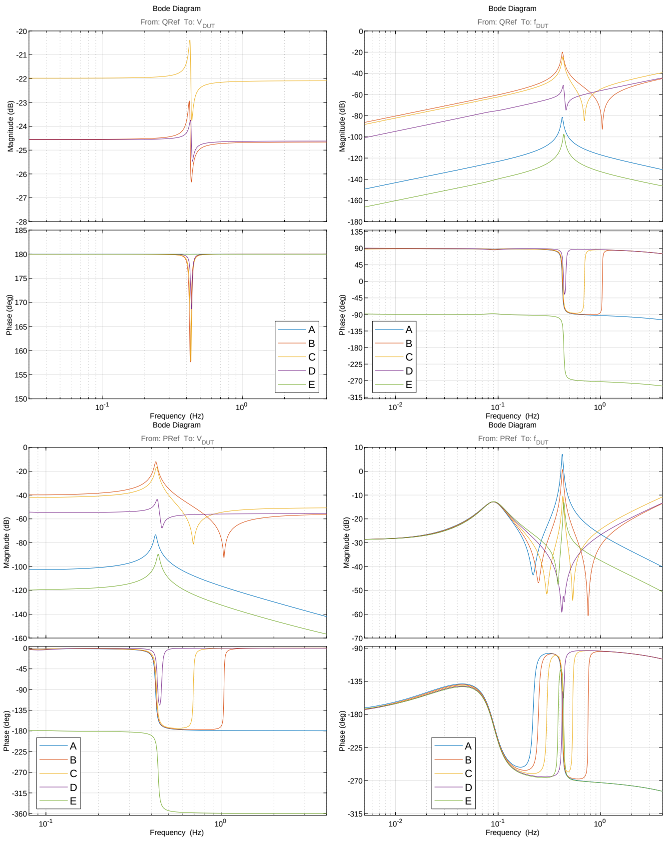

Fig. 5: Freq. resp.: on top, from Q_{DUT}^{ref} to V_{DUT} (left), to f_{DUT} (right). On bottom, same thing from P_{DUT}^{ref}.

First, the top left figure in Fig. 5 shows that a POD-Q(V) structure is the most challenging case. Indeed, whatever the scenario, the resonance and anti-resonance frequencies are very close, which makes it difficult to design an efficient controller that is also robust to the uncertainty in the resonance and anti-resonance frequencies. A small mistake in the resonance and anti-resonance frequencies' value can compromise the sought properties in closed-loop, particularly the stability.

In Fig. 6, the computed JCOL and RJCOL indexes are reported. They highlight the best scenarios in a control point of view for a given POD control strategy. In particular, as anticipated, cases A and E are deemed irrelevant from both controllability and observability perspectives. Then, the top right figure in Fig. 5 shows that there is no anti-resonance in the transfer function from Q_{DUT}^{ref} to f_{DUT}. Hence, only the JCOL index can be used.

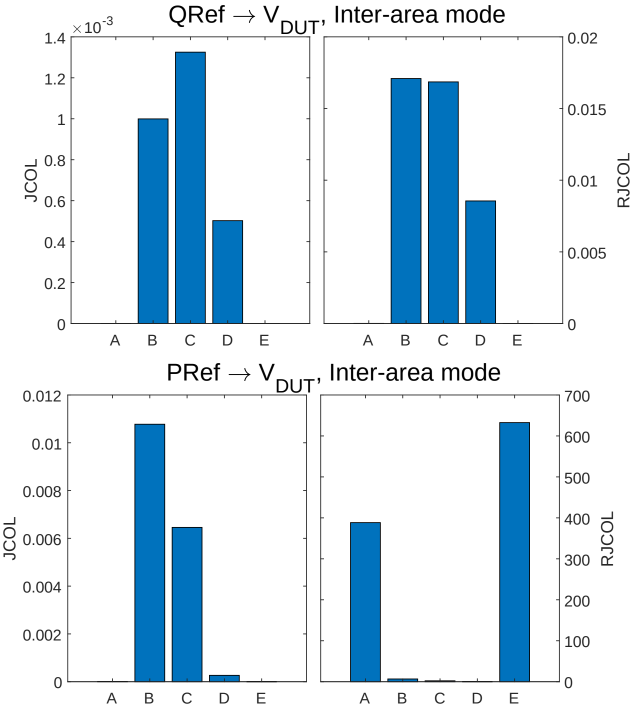

Fig. 6: JCOL (left) and RJCOL (right) indexes of the inter-area mode for the transfer function Q_{DUT}^{ref} to V_{DUT} (top), and P_{DUT}^{ref} to V_{DUT} (bottom).

Fig. 7 shows the JCOL indexes of the inter-area mode for both transfer functions linking the inputs Q_{DUT}^{ref} and P_{DUT}^{ref} to the output f_{DUT}. Fig. 5 concern the transfer functions from P_{DUT}^{ref} to V_{DUT} and f_{DUT}, respectively.

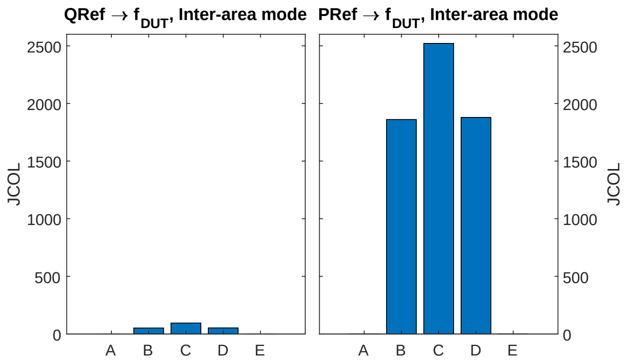

Fig. 7: JCOL indexes of the IZ mode for the transfer function Q_{ref} to f_{DUT} (left), and P_{ref} to f_{DUT} (right).

A POD-P(f) strategy will be more efficient from a control design point of view than a POD-Q(f) one, especially for scenarios A, B, C and E. The scenario D does not control or observe the inter-area mode frequency, it is thus disqualified for the POD-P(f) strategy. The scenarios A and E can be ignored since they have a very weak influence on the voltage. Scenarios B and C remain acceptable and better than any scenario involving a POD-Q(f) strategy. If a POD-Q(f) strategy is chosen, the JCOL shows good results for B and C cases, the case D being, to a lesser extent, also acceptable.

4 POD controller design

In this section, several tunings for various control strategies are considered to get an inter-area mode damping that is as satisfying as possible. Of course, the closed-loop performances should meet the actual requirements of RTE and raise new ones in order to better guide the manufacturers. In the sequel, we shall design the POD with a linearised model of scenario B, as it appears to be a good trade-off during the analysis of the controllability and observability of the inter-area mode in Section 3.

4.1 POD design applying RTE margin requirements

The robustness requirements are expressed in terms of Modulus and Complementary Modulus margins, M_m and M_{mc}, as well as in term of Delay margin Δ_τ, as recalled in Section 1. Following this, the different proposed POD controllers are set using a loop-shaping approach [18], using the Nichols diagram on which we report the Modulus and Complementary Modulus margins as areas that encircle the stability critical point that are not to cross.

4.1.1 POD-P(f) case: The examination of modal controllability and observability in Section 3 has highlighted the superiority of this control strategy with respect to the other ones. The better tunings (but not the optimised ones) are obtained with the following controller

$$C_P(s) = K_{POD,P}\, WO_P(s)\, R_P(s),$$

with the following control law

$$P_{ref}(s) = +C_P(s)\, f_{DUT}(s) + \gamma_P\, P^*_{ref}(s),$$

where $P^*_{ref}(s)$ is the active power reference signal, f_{DUT} is the measured frequency at PCC, and γ_P is a gain allowing the adjustment of the closed-loop static gain in a transfer function of interest. The parameters have been set to $K_{POD,P} \simeq 17.78$, $T_{WO,P} \simeq 3.1831$, $\xi_{r,P} = 7$ and $\omega_{r,P} \simeq 125.66$ while $T_{lp,P} = T_{1,P} = T_{2,P} = 0$.

4.1.2 POD-Q(f) case: The examination of modal controllability and observability in Section 3 has highlighted the strength of this control strategy with respect to POD-Q(V) but also its weakness with respect to POD-P(f).

The better tunings (but also not the optimised ones) are obtained with the following controller

$$C_Q(s) = K_{POD,Q}\, WO_Q(s)\, R_Q(s),$$

with the following control law

$$Q_{ref}(s) = -C_Q(s)\, f_{DUT}(s) + \gamma_Q\, Q^*_{ref}(s),$$

where $Q^*_{ref}(s)$ is the reactive power reference signal, f_{DUT} is the measured frequency at PCC, and γ_Q is a gain allowing the adjustment of the closed-loop static gain for a transfer function of interest. The parameters have been set to $K_{POD,Q} \simeq 100.0$, $T_{WO,Q} \simeq 3.1831$, $\xi_{r,Q} = 2$ and $\omega_{r,Q} \simeq 94.2478$ while $T_{l,Q} = T_{1,Q} = T_{2,Q} = 0$.

4.1.3 POD-Q(V) case: This control strategy appears to be challenging in damping the inter-area oscillation mode because of the weak indexes of JCOL/RJCOL observed in Fig. 6. The better tunings (but also not the optimised ones) are obtained with the following controller

$$C_{Qv}(s) = K_{POD,Qv}\, WO_{Qv}(s)\, PC_{Qv}(s)\, R_{Qv}(s),$$

with the following control law

$$Q_{ref}(s) = +C_{Qv}(s)\, V_{DUT}(s) + \gamma_{Qv}\, Q^*_{ref}(s),$$

where $Q^*_{ref}(s)$ is the reactive power reference signal, V_{DUT} is the measured voltage at PCC, and γ_{Qv} is a gain allowing the adjustment of the closed-loop static gain for a transfer function of interest. The parameters have been set to $K_{POD,Qv} \simeq 10.0$, $T_{WO,Qv} \simeq 0.96458$, $\xi_{r,Qv} = 0.01606$ and $\omega_{r,Qv} \simeq 2.6806$, $T_{1,Qv} \simeq 1.169$, $T_{2,Q} \simeq 0.067877$, while $T_{l,Qv} = 0$.

4.2 Performance verification on linearised model

In this section, the closed-loop performance and robustness of the proposed solutions in both the time and frequency domains are assessed, starting with the same linearised model used for the control design.

4.2.1 POD-P(f) case: The closed-loop performances, in terms of damping of the inter-area oscillation mode in the response of f_{DUT}, can be evaluated in Fig. 9. More than 20 dB of reduction is obtained on the peak of resonance of the inter-area mode, but also roughly 15 dB of reduction on a low-frequency peak of resonance at $\simeq 0.09\ Hz$. Regarding the voltage at the DUT terminals, Fig. 10, top and bottom, shows the time responses of this voltage to a step of $-0.05\ pu$ on P_{ref} and on Q_{ref} respectively. Fig. 8 expresses the meeting of Modulus and Complementary modulus margins since the Nichols plot stays outside the required areas. Their computations give $M_m \simeq 0.915$ and $M_{mc} \simeq 1.03$, respectively. The computation of the delay margin gives $\Delta\tau \simeq 398\ ms$. All these margins are far beyond RTE's actual requirements.

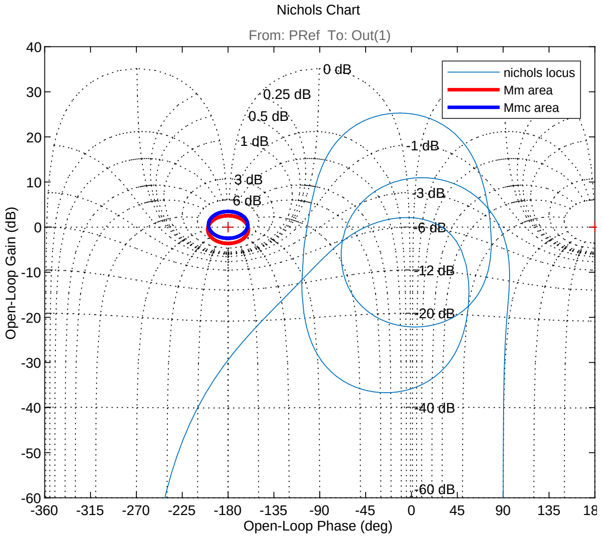

Fig. 8: Frequency response of the open-loop transfer function for the POD-P(f) controller.

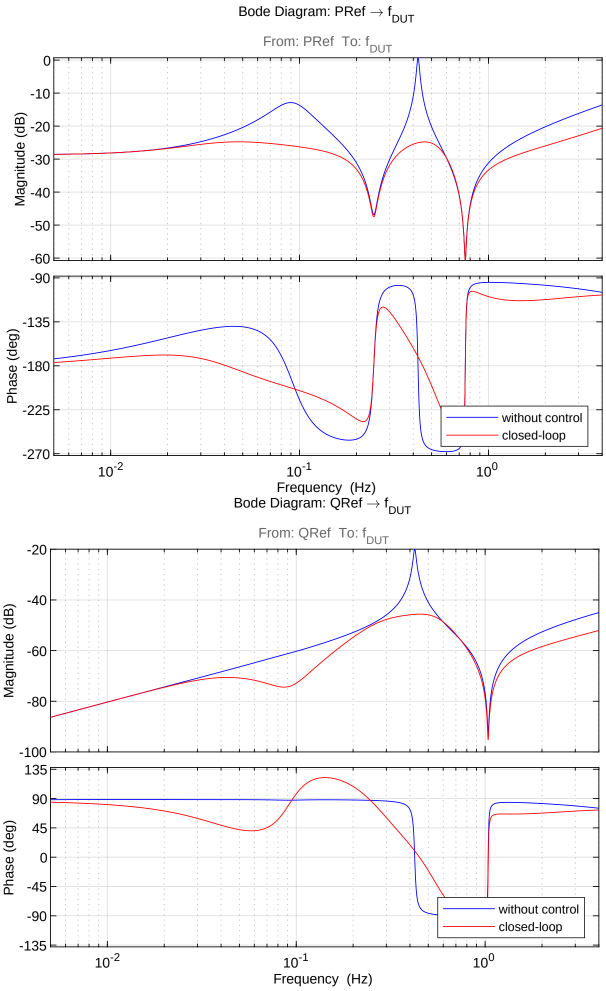

Fig. 9: Frequency responses of the transfer functions from P_{ref} to f_{DUT} (top) and from Q_{ref} to f_{DUT} (bottom), without control (blue) and in closed-loop (red) with the POD-P(f) controller.

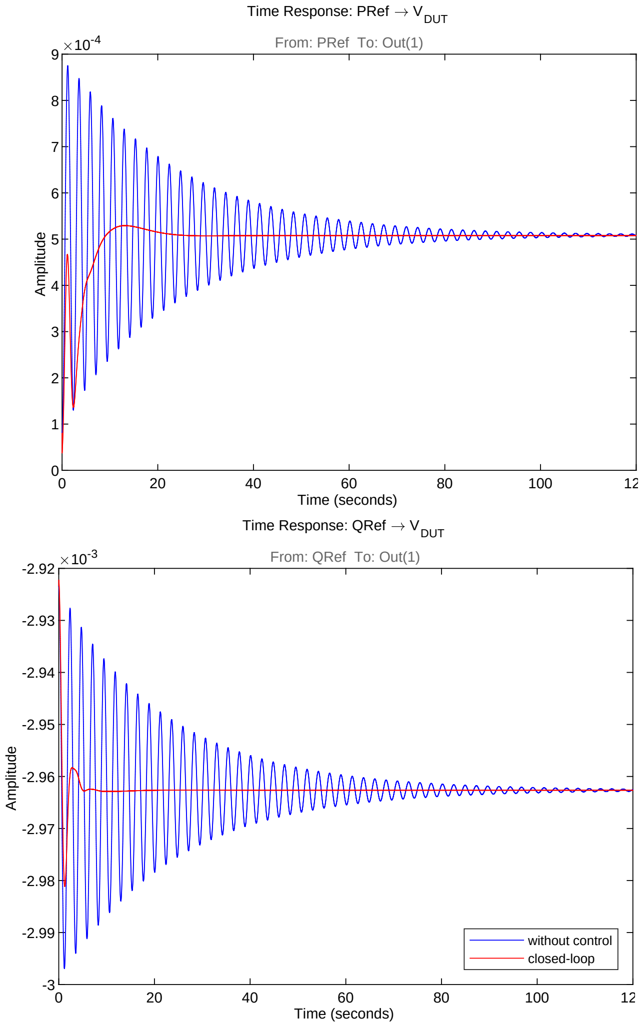

Fig. 10: $-0.05\ pu$ step responses of the transfer functions from P_{ref} to V_{DUT} (top) and from Q_{ref} to V_{DUT} (bottom), without control (blue) and in closed-loop (red) with the POD-P(f) controller.

4.2.2 POD-Q(f) case: The closed-loop performances are examined following the same approach as for the previous POD-P(f) controller. In terms of damping of the inter-area mode in the response of f_{DUT}, it can be evaluated in Fig. 12. Almost 20 dB of reduction is obtained on the peak of resonance of the inter-area mode, but this time, the low-frequency peak of resonance at $\simeq 0.09\ Hz$ remains unchanged. This is due to the low value of the RJCOL for this mode, meaning it is nearly uncontrollable by Q_{ref} and/or unobservable by f_{DUT}.

The time responses of the voltage at the DUT terminals to a step of $-0.05\ pu$ on P_{ref} and on Q_{ref} is shown in Fig. 13, on left and on right, respectively.

Fig. 11 expresses the satisfying Modulus and Complementary modulus margins since the Nichols plot stays outside the required areas. Their computations give $M_m \simeq 0.522$ and $M_{mc} \simeq 0.899$, respectively. The computation of the delay margin gives $\Delta\tau \simeq 525\ ms$. Again, all these margins meet the specifications expected by RTE.

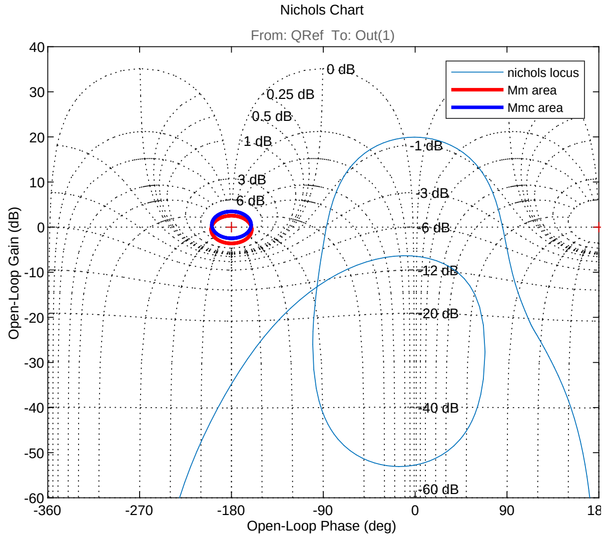

Fig. 11: Frequency response of the open-loop transfer function for the POD-Q(f) controller.

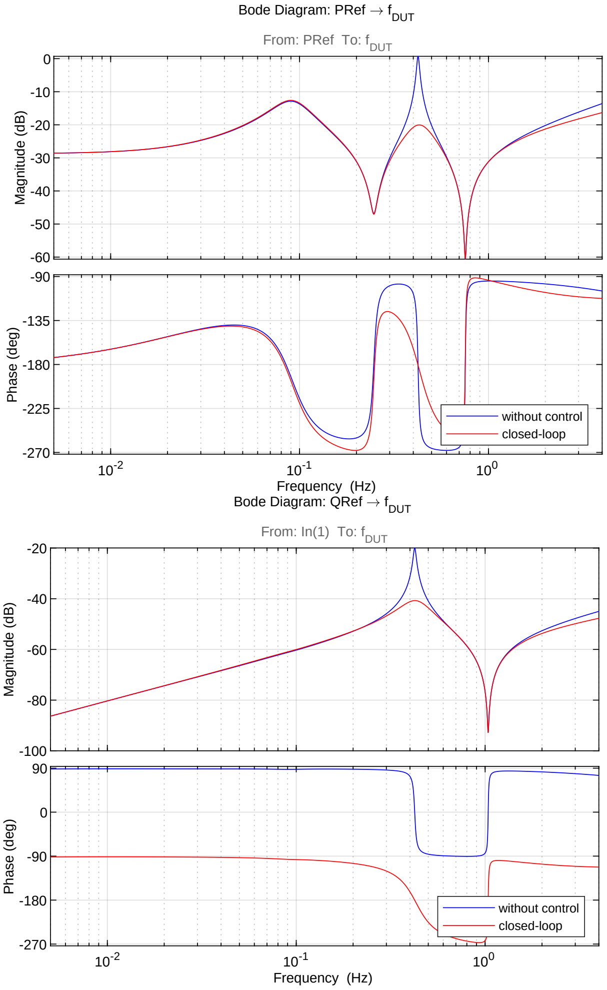

Fig. 12: Frequency responses of the transfer functions from P_{ref} to f_{DUT} (top) and from Q_{ref} to f_{DUT} (bottom), without control (blue) and in closed-loop (red) with the POD-Q(f).

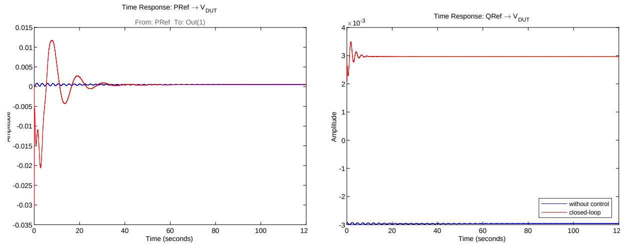

Fig. 13: $-0.05\ pu$ step responses of the transfer functions from P_{ref} to V_{DUT} (left) and from Q_{ref} to V_{DUT} (right), without control (blue) and in closed-loop (red) with the POD-Q(f) controller.

4.2.3 POD-Q(V) case: The damping of the inter-area mode in the response of f_{DUT} can be evaluated in Fig. 14. Almost $40\ dB$ of reduction is obtained on the peak of resonance of the inter-area mode in this figure. The low-frequency peak of resonance at $\simeq 0.09\ Hz$ remains unchanged since it is nearly uncontrollable by Q_{ref} and/or unobservable by V_{DUT}. Fig. 15 expresses the satisfying Modulus and Complementary modulus margins since the Nichols plot stays outside the required areas. Their computations give $M_m \simeq 0.838$ and $M_{mc} \simeq 1.01$, respectively. The computation of the delay margin gives $\Delta\tau \simeq 216\ ms$. Again, all these margins meet the specifications expected by RTE.

One should pay attention to the closed-loop transfer function between P_{ref} and f_{DUT} that is not affected at all by the POD-Q(V) controller as shown by the frequency response on the top of Fig. 14. It could be either due to an inappropriate design and/or setting of the POD-Q(V) as specified by the control structure of Subsection 2.3, or an inherent feature of this control strategy that could not be adequate to the considered system. Further investigations will be conducted in future work. A more efficient strategy, based on closed-loop pole placement, has been done for this control structure, but it led to an intrinsically unstable controller, although satisfying the expected performances on the inter-area mode damping. The corresponding results are omitted, as intrinsically unstable controllers should not be implemented in critical systems like power grids, since sensor malfunctions in the feedback loop could result in significant system failures.

5 POD performance assessment

In this section, the damping contribution of each solution is quantified through eigenvalue analysis, and robustness tests are performed using the original nonlinear model in OpenModelica [19]. The POD-Q(V) will not be discussed further, as the current design has proven ineffective in the proposed benchmark despite complying with RTE stability margin requirements.

5.1 Reducing the gain to limit the DUT response

Tabs. 1 and 2 demonstrate that both POD-P and POD-Q, based on the frequency measurement, contribute positively to system damping. However, their effectiveness diminishes as the gain is

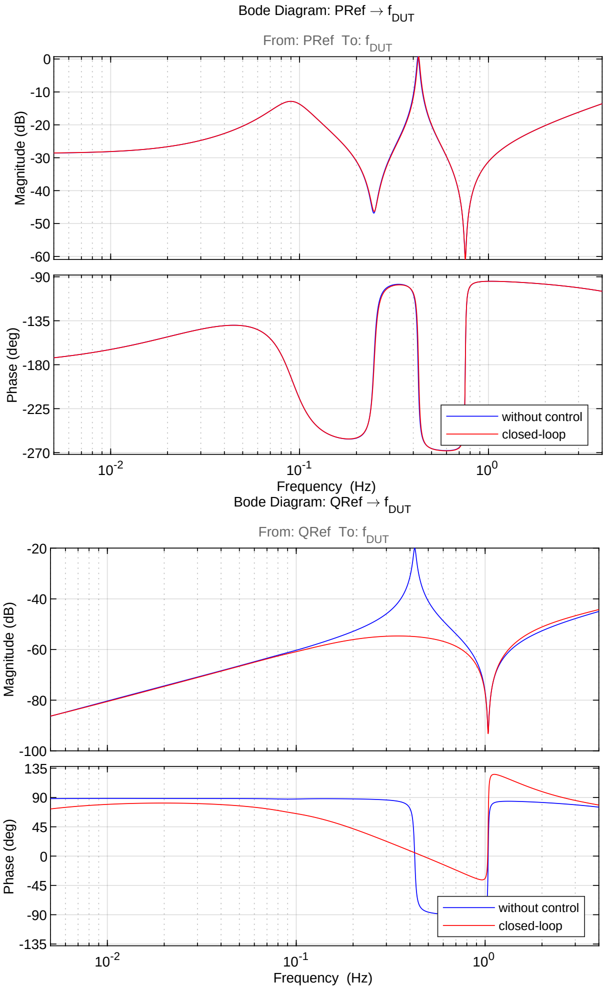

Fig. 14: Frequency responses of the transfer functions from P_{ref} to f_{DUT} (top) and from Q_{ref} to f_{DUT} (bottom), without control (blue) and in closed-loop (red) with the POD-Q(V) controller.

decreased to maintain the power response within realistic values, as shown in Figs. 16 and 17. In the following, the reduced gain value will be considered.

Table 1 Effect on inter-area mode and associated damping of different values of POD-P(f) gains

Case	f (Hz)	ζ (%)
wo POD	0.42	1.61
with POD - K	0.55	30.15
with POD - K/10	0.42	4.59
with POD - K/25	0.42	2.79

5.2 *Parametric robustness*

Tabs. 3 and 4 illustrate how the damping contribution diminishes when the PCC location is shifted along the line between the two IGs, except for POD-P(f) and α=0.1. In some cases, the damping drops below the initial value, indicating that the DUT introduces negative damping, which may be deemed unacceptable. Regarding the total length between the two inertial grids, which affects the mode frequency, both controllers demonstrate good robustness (see Tab. 5). The same property is observed when considering a radial connection line (see Tab. 6).

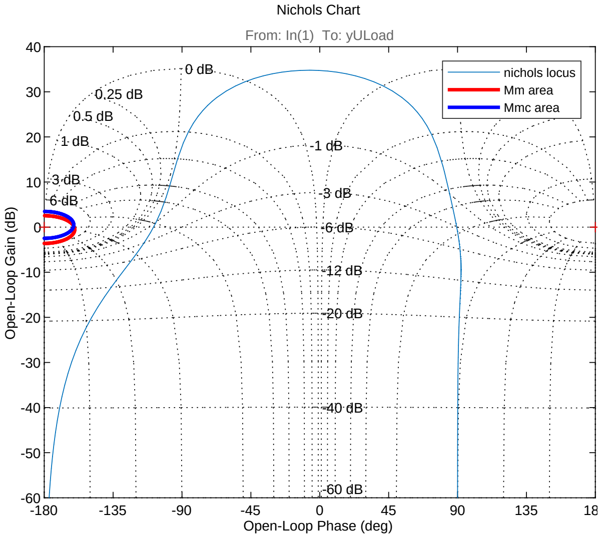

Fig. 15: Frequency response of the open-loop transfer function for the POD-Q(V) controller.

Table 2 Effect on inter-area mode and associated damping of different values of POD-Q(f) gains

Case	f (Hz)	ζ (%)
wo POD	0.42	1.61
with POD - K	0.43	18.54
with POD - K/10	0.42	3.24
with POD - K/25	0.42	2.26

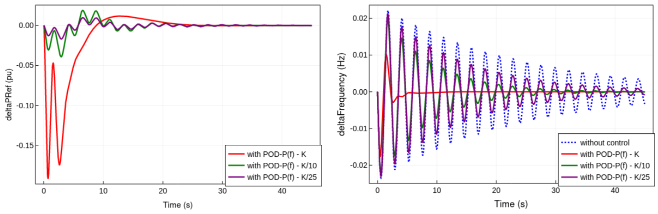

Fig. 16: POD-P(f) response (left) and effect on the inter-area mode (right) for an active power step (25 MW) at PCC A

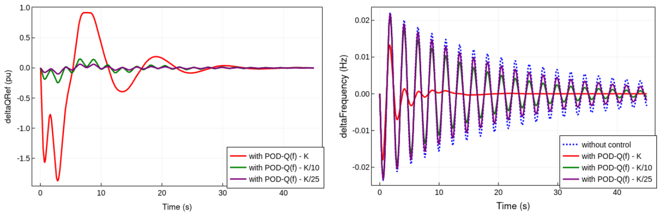

Fig. 17: POD-Q(f) response (left) and effect on the inter-area mode (right) for an active power step (25 MW) at PCC A

Table 3 Effect on inter-area mode and associated damping of different locations of DUT with POD-P(f)

α	ζ - wo control (%)	ζ - with POD (%)	$\Delta\zeta$ (%)
0.1	1.62	3.55	**1.93**
0.25	1.61	2.79	**1.18**
0.5	1.60	1.92	**0.32**
0.75	1.58	1.58	**0**
0.9	1.57	1.64	**0.07**

Table 4 Effect on inter-area mode and associated damping of different locations of DUT with POD-Q(f)

α	ζ - wo control (%)	ζ - with POD (%)	$\Delta\zeta$ (%)
0.1	1.62	2.05	**0.43**
0.25	1.61	2.26	**0.65**
0.5	1.60	1.99	**0.39**
0.75	1.58	1.59	**0.01**
0.9	1.57	1.52	**-0.05**

5.3 Robustness to the operating point

Finally, Tab. 7 shows that POD-P(f) consistently maintains performance across a range of operating conditions, whereas POD-Q(f) fails to provide positive damping as the system operating point changes. OP 2 represents a power flow inversion for IG 2 to IG 1, while in OP 3 no power exchange with IG 2. This highlights the relevance of incorporating diverse scenarios in compliance verification, as is commonly specified.

6 Discussions, conclusion and future work

6.1 On the trade-off between performance and robustness

While performance requirements are important, they should not outweigh the risk of compromising system SSS in specific scenarios. The baseline expectation remains **positive damping** over a defined frequency range across the broadest set of possible operating conditions; the DUT must not, under any circumstances, deteriorate system damping. The desired level of contribution to the damping of inter-area modes may vary depending on the technology. TSO-owned assets, such as HVDC systems and FACTS, or large facilities in general, could strive to maximise performance, while distributed PPMs should prioritise robustness. With this trade-off in mind, all grid-connected devices should contribute as much as possible, even if their impact seems marginal at a given time, as it may become critical in different scenarios. Future efforts will focus on refining these requirements and setting relevant test cases that encourage good performance levels while ensuring robustness. This approach should cover not only diverse operating conditions but also the various low-frequency electromechanical modes that may suffer from low damping.

6.2 On the limits and opportunities of more detailed compliance verification benchmarks

This work presented an in-depth analysis of a two-area benchmark, designed to replicate inter-area modes, highlighting both the opportunities and limitations of its use in verifying POD compliance. A thorough controllability and observability analysis showcased the ability of the reduced equivalent model to capture the limited effect of the DUT on the system dominant mode in specific cases—particularly when using voltage measurements tightly regulated by voltage sources or when the DUT is located close to the system COI. That said, simplified models considered in this work may require further refinement to adequately assess the contributions of POD-Q(V) type solutions, such as including voltage dependent loads.

More importantly, it has been demonstrated that leveraging embedded information beyond mode frequency—illustrated here by the JCOL—may lead to solutions that, despite exhibiting excellent time-domain performance in the specific test settings, could lack robustness and even stability in different operating conditions, demonstrating that **frequency-domain requirements remain indispensable** and further work is need on their refinement. Other key takeaways include:

- One limitation of equivalents is that *you get out what you put in*, making it essential to thoroughly understand the underlying assumptions before setting compliance criteria.
- While grid access requirements aim to be non-discriminatory, the physical phenomena at play are not.

6.3 On POD controllers design

Tackling the oscillation damping of low-frequency modes in the considered power system is not an easy task, especially when using only SISO-type controllers for a MIMO system involving several dynamics that are all coupled with all the control inputs. If one can manage to control one input-output channel of such a MIMO system, the coupling effects could raise undesired behavior in the other channels, resulting in a global closed-loop system that could not meet the expected requirements in terms of performance and robustness.

The POD-Q(V) case has shown that even if all the requirements were satisfied in terms of inter-area mode damping and robustness margins for the Q_{ref} to V_{DUT} channel, it could not provide a similar behavior for the channels of interest, say from P_{ref} to V_{DUT} and from P_{ref} to f_{DUT}, showing that the actual requirements need to be carefully specified to reject such controller. Moreover, the *strong stability* issue should be explicitly addressed to avoid unstable controllers, although they could be efficient. However, this problem is known to be hard to tackle as it is highly nonlinear in the design parameters. It is still a major scope that mobilises researchers in the automatic control field. Other works have shown the benefit of using *optimal control design* methods like the $\mathcal{H}_\infty$ synthesis as reported in [20] and related works. More generally, using MIMO controllers combined with robust and optimal design methods as proposed in [18, 21, 22] could be helpful in getting efficient POD controllers. The MIMO-type controllers could also be exploited to

Table 5 Effect of different distances between the two IGs

L1+L2	Without Control		POD-P(f)			POD-Q(f)		
	f (Hz)	ζ (%)	f (Hz)	ζ (%)	$\Delta\zeta$ (%)	f (Hz)	ζ (%)	$\Delta\zeta$ (%)
1000 kms	0.53	1.25	0.53	2.12	**1.59**	0.53	1.58	**1.05**
1500 kms (original case)	0.42	1.61	0.42	2.79	**1.18**	0.42	2.26	**0.65**
2000 kms	0.35	2.02	0.35	3.54	**1.52**	0.35	3.12	**1.10**

Table 6 Effect of a radial connection for the DUT

L3	Without Control		POD-P(f)			POD-Q(f)		
	f (Hz)	ζ (%)	f (Hz)	ζ (%)	$\Delta\zeta$ (%)	f (Hz)	ζ (%)	$\Delta\zeta$ (%)
0 km (original case)	0.42	1.61	0.42	2.79	**1.18**	0.42	2.26	**0.65**
500 kms	0.42	1.62	0.42	2.80	**1.18**	0.42	2.27	**0.65**
1000 kms	0.42	1.63	0.42	2.81	**1.18**	0.42	2.26	**0.64**

Table 7 Effect of different operating points

Operating Point	Without Control		POD-P(f)			POD-Q(f)		
	f (Hz)	ζ (%)	f (Hz)	ζ (%)	$\Delta\zeta$ (%)	f (Hz)	ζ (%)	$\Delta\zeta$ (%)
OP1 (original case)	0.42	1.61	0.42	2.79	**1.18**	0.42	2.26	**0.65**
OP2	0.38	1.84	0.38	3.28	**1.44**	0.38	0.36	**-1.48**
OP3	0.44	1.54	0.44	2.61	**1.07**	0.44	1.46	**-0.05**

set a smarter distributed control effort between P_{ref} and Q_{ref} since the first one is more able to act on the system's dynamic rather than the second, but at the same time, it is considered as a precious quantity not to be too much shaken for stability purposes. The robust and optimal control methods require a specific mathematical formulation, carefully addressed in order to derive more relevant TSO requirements.

In general, the control community has developed several robust and optimal control techniques that could be helpful in designing efficient POD controllers. For example, one could specify a pole placement region in the complex plane relevantly defined to cope with the desired behaviour, simultaneously with a minimisation of the norm of an input-output channel expressing a disturbance rejection requirement, as proposed in [23] for the active vibration damping of mechanical structures. It could lead to avoiding obtaining the previous POD-Q(V) controller that met current RTE requirements but turned out to be poorly efficient. Moreover, the limits on control signals could also be addressed by using *anti-windup compensators* combined with robust and optimal controllers, as in [24].

7 References

[1] F. J. De Marco, N. Martins, and J. C. R. Ferraz, "An automatic method for power system stabilizers phase compensation design," *IEEE Transactions on Power Systems*, vol. 28, no. 2, pp. 997–1007, 2013.

[2] J. Renedo, L. Sigrist, and L. Rouco, "Design of power system stabilizers to damp low frequency inter-area oscillations with limited information," in *2019 IEEE Milan PowerTech*, pp. 1–6, 2019.

[3] RTE, "Documentation technique de référence," 2023.

[4] I. PES, "Ieee tutorial course power system stabilization via excitation control," 2009.

[5] "Ieee guide for identification, testing, and evaluation of the dynamic performance of excitation control systems," *IEEE Std 421.2-2014 (Revision of IEEE Std 421.2-1990)*, pp. 1–63, 2014.

[6] J. Renedo, A. Díaz-García, G. Torresan, E. Lorenzo, A. Cordón, S. Sanz, J. Peiró, J. Pérez, G. Calvo, A. Hernández, A. Petit, H. Oukhayi, S. Akkari, and H. Saad, "Tests on the pod-p controller of inelfe spain-france vsc-hvdc interconnector," in *B4 International SC Meeting and Colloquium*, vol. 2023, pp. 1–15, 2023.

[7] ENTSOE, "Analysis of ce inter-area oscillations of 1 st december 2016," 2017.

[8] ENTSOE, "Oscillation event 03.12.2017," 2018.

[9] L. Petersen, P. H. Nielsen, and G. C. L. T. Tarnowski, "Addressing power oscillations damping requirements for wind power plants," in *20th Wind & Solar Integration Workshop*, 2021.

[10] C. R. (EU), "2016/631 of 14 april 2016 establishing a network code on requirements for grid connection of generators," 2016.

[11] R. Ogiewa, "The practical importance of clear grid code requirements and stakeholder involvement in the context of large- scale grid integration of wind power in sweden," in *22nd Wind & Solar Integration Workshop*, 2023.

[12] P. Anderson and M. Mirheydar, "A low-order system frequency response model," *IEEE Transactions on Power Systems*, vol. 5, no. 3, pp. 720–729, 1990.

[13] C. Cardozo, A. Diaz-Garcia, G. Giannuzzi, G. Torresan, F. Xavier, A. Cordón, L. Coronado, R. Zaottini, and C. Pisani, "Small signal stability analysis of the angle difference control on a hvdc interconnection embedded in

the ce synchronous power system," in *2020 IEEE/PES Transmission and Distribution Conference and Exposition (T&D)*, pp. 1–5, 2020.

[14] V. Costan, C. Cardozo, and P. Rault, "Assessing the subsynchronous damping capability of an hvdc link using grid-forming control," in *23rd Wind & Solar Integration Workshop*, 2024.

[15] H. Pulgar-Painemal, Y. Wang, and H. Silva-Saravia, "On inertia distribution, inter-area oscillations and location of electronically-interfaced resources," *IEEE Transactions on Power Systems*, vol. 33, no. 1, pp. 995–1003, 2018.

[16] S. Chan, "Modal controllability and observability of power-system models," *Int. Journal of Electrical Power & Energy Systems*, vol. 6, no. 2, pp. 83–88, 1984.

[17] A. Hamdan and A. Elabdalla, "Geometric measures of modal controllability and observability of power system models," *Electric Power Systems Research*, vol. 15, no. 2, pp. 147–155, 1988.

[18] S. Skogestad and I. Postlethwaite, *Multivariable Feedback Control: Analysis and Design*. Wiley, 2005.

[19] P. Fritzson, A. Pop, K. Abdelhak, A. Ashgar, B. Bachmann, W. Braun, D. Bouskela, R. Braun, L. Buffoni, F. Casella, R. Castro, R. Franke, D. Fritzson, M. Gebremedhin, A. Heuermann, B. Lie, A. Mengist, L. Mikelsons, K. Moudgalya, L. Ochel, A. Palanisamy, V. Ruge, W. Schamai, M. Sjölund, B. Thiele, J. Tinnerholm, and P. Östlund, "The OpenModelica Integrated Environment for Modeling, Simulation, and Model-Based Development," *Modeling, Identification and Control*, vol. 41, no. 4, pp. 241–295, 2020.

[20] Y. Xing, *Commande des liaisons à courant continu (HVDC) pour l'amortissement des oscillations interzones*. PhD thesis, 2021. Thèse de doctorat dirigée par Marinescu, Bogdan Automatique, productique et robotique Ecole centrale de Nantes 2021.

[21] K. Zhou, J. Doyle, and K. Glover, *Robust and Optimal Control*. Feher/Prentice Hall Digital and, Prentice Hall, 1996.

[22] D. Alazard, C. Cumer, P. Apkarian, M. Gauvrit, and G. Ferrères, *Robustesse et commande optimale*. Cépaduès-éd., 1999.

[23] S. Tliba, "Control of a Vibrating Axisymmetric Membrane Using Piezoelectric Transducers," in *18th IFAC World Congress*, (Milano, Italy), p. 7713 (6 pages), Aug. 2011.

[24] S. Tliba, "Vibration damping of a flexible beam with saturated control," in *2012 American Control Conference (ACC)*, pp. 5330–5335, 2012.

A Background on stability margins

The more widespread stability margins are the gain and phase margins, which can be computed either numerically or by a simple inspection of Nyquist, Nichols or Bode diagrams. They provide insight on the system's robustness. Furthermore, the well-known Nyquist criterion states that the closed-loop system is stable if and only if the plot of the open-loop system's frequency response in the Nyquist chart surrounds the point of affix -1 (the critical point, denoted by C in the sequel, see Fig. 18), a number of times equal to the number of unstable poles of the open-loop system.

Let $s \in \mathbb{C}$ be the Laplace variable and $L_0(s)$ be the open-loop TF of the system. It corresponds to the product of the TF of the system, say $G(s)$, and the controller, say $K(s)$. Then:

The *gain margin* is $\Delta G := \dfrac{1}{|L_0(j\omega_{-\pi})|}$ with $\omega_{-\pi}$ corresponding to the frequency for which $\arg L_0(j\omega_{-\pi}) = -\pi$. The frequency $\omega_{-\pi}$ may be not unique, depending on the number of intersections between the Nyquist plot and the real axis. When considering the two closest intersections overlapping the critical point C along the real axis (see Fig. 18), then we can define the increasing gain margin ΔG_m and the decreasing gain margin ΔG_d. These indicators inform about the pure gain uncertainty the closed-loop may tolerate before instability.

The *phase margin* is $\Delta\varphi := \arg\{L_0(j\omega_0)\} - (-\pi)$ with ω_0 corresponding to the frequency of unit modulus, *i.e.* for which $|L_0(j\omega_{-\pi})| = 1$. The frequency ω_0 may be not unique, depending on the number of intersections between the Nyquist plot and the unitary circle. When considering the two closest intersections overlapping the critical point C along the red circle (see Fig. 18), then we can define the lead phase margin $\Delta\varphi_a$ and the lag phase margin $\Delta\varphi_r$.

The usual *delay margin* is derived from the phase margin and given by $\Delta\tau := \frac{\Delta\varphi}{\omega_0}$, and also $\Delta\tau_r := \frac{\Delta\varphi_r}{\omega_{0r}}$, $\Delta\tau_a := \frac{\Delta\varphi_a}{\omega_{0a}}$ when dealing with lead and lag phase margins respectively.

The *modulus margin* is $M_m := (\|\mathcal{S}(j\omega)\|_\infty)^{-1}$ at the frequency ω_m, where $\mathcal{S}(j\omega) := \frac{1}{1+L_0(j\omega)}$ is the *output sensitivity TF*. From a practical viewpoint, it is the shortest distance between the Nyquist plot of $L_0(j\omega)$ and the critical point C, say the radius of the blue circle on Fig. 18.

The *complementary modulus margin* is given by: $M_{mc} := (\|\mathcal{T}(j\omega)\|_\infty)^{-1}$ at the frequency ω_{mc}, where $\mathcal{T}(j\omega) := \frac{L_0(j\omega)}{1+L_0(j\omega)}$ is the *complementary output sensitivity TF*, $1/M_m$ and $1/M_{mc}$ stand for the $\mathcal{H}_\infty$ norm of $\mathcal{S}(j\omega)$ and $\mathcal{T}(j\omega)$ respectively, see [18].

From a practical viewpoint, $1/M_{mc}$ is the highest gain value of the frequency response of $\mathcal{T}(s)$ and $1/M_m$ is the highest gain value of $\mathcal{S}(s)$.

Interpretation of RTE robustness requirement: according to these definitions and geometrical properties, RTE's margins imply the guarantee of the following inequalities for the decreasing and increasing gain margins, respectively

$$\Delta G_{ddB} < -3.48\, dB, \qquad \Delta G_{mdB} > 3.61\, dB,$$

and the following inequalities for the lead and lag phase margins

$$\Delta\varphi_a,\ \Delta\varphi_r \geq \max(19.576\, deg, 18.994\, deg).$$

The corresponding delay margins depend on the unitary frequencies at which occurs the intersection of the Nyquist plot of $L_0(j\omega)$ and the unitary circle.

Table 8 Eigenvalues for different two-IGs system variants

Case	λ_1,λ_2	λ_3,λ_4	λ_5	λ_6	$f_{\lambda_{3,4}}$ (Hz)	$\zeta_{\lambda_{3,4}}$ (%)
A	-0.14 ± j0.56	-0.043 ± j2.65	-0.19	0	0.422	1.62
B	-0.14 ± j0.55	-0.043 ± j2.66	-0.19	0	0.424	1.61
C	-0.14 ± j0.55	-0.043 ± j2.69	-0.19	0.0	0.428	1.6
D	-0.14 ± j0.56	-0.043 ± j2.72	-0.19	0.0	0.43	1.57
E	-0.14 ± j0.55	-0.042 ± j2.74	-0.19	0	0.43	1.56

Table 9 Initial operating point per scenario

Case	$Q_{1,0}(Mvar)$	$U_{2,0}$ (pu)	$\theta_{2,0}$ (rad)	$U_{3,0}$ (pu)	$\theta_{3,0}$ (rad)
A	31.3	1.023	-0.30	1.072	0
B	13.25	1.045	-0.18	1.048	-0.10
C	19.5	1.033	-0.23	1.045	-0.07
D	25.7	1.025	-0.27	1.053	-0.03
E	7.29	1.06	-0.14	1.06	-0.14

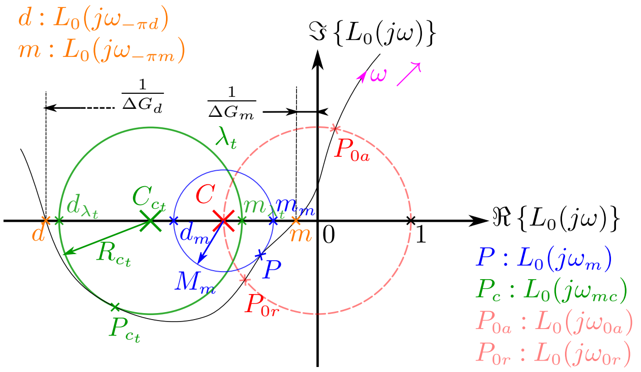

Fig. 18: Different stability margins in the Nyquist plot, case where $\lambda_t := \dfrac{1}{M_{mc}} > 1$.

It is worth mentioning that the usual gain and delay margins inform about pure gain uncertainty or pure delay uncertainty, each separately affecting the open-loop system before the closed-loop becomes unstable. In no case should one combine this information to draw conclusions about the robustness of the closed-loop for both simultaneous uncertainties extracted from these margins. On the contrary, the modulus margin allows us to account for the worst-case scenario of combined uncertainties in both gain and delay of the open-loop system. Therefore, using this indicator for compliance is quite relevant from a conservatism perspective. Finally, regarding the very less established notion of *complementary modulus margin*, it allows us to account for downwards gain uncertainties.

B Model linearisation and validation

B.1 Deriving state-space models in Modelica

State-space models are obtained by using the linearisation option provided by OpenModelica. This linearisation is a numerical one, making use of the Jacobian matrix available at the current time step. Inputs and outputs can be directly defined in the Modelica test case.

B.2 Eigenvalue analysis of the two-IGs system

Table 8 demonstrates that the dynamic properties of the two-IGs are maintained when transitioning from one variant to another and that the mode of interest ($\lambda_{3,4}$) is poorly damped.

C Model parameters

The total distance between the IGs (L_{tot}) is 1500 km. For Case B ($\alpha = 0.25$), the DUT PCC is located 375 km from IG 1, while for Case D ($\alpha = 0.75$), the PCC is positioned 1125 km from IG 1 (and 375 km from IG 2). Considering a x_l, of 0.35 Ω/km, the reactance values used in this work are 131.25 Ω, 262.5 Ω, and 393.75 Ω when accounting for 25%, 50%, and 75% of the total value, respectively. Regarding the initial operating points, Tab. 9 provides the PF solution for the different scenarios. Since resistances are neglected, IG 1 consistently produces exactly 50 MW in all scenarios. Finally, Tab. 10 includes the IGs parameters.

Table 10 Two-IGs test system parameters (based on [2])

Parameter	IG 1	IG 2
Base power (S_n, MVA)	1500	5000
Base voltage (U_n, kV)	400	400
Base impedance (Z_{base}, Ω)	106.67	32
Reheater time constant (T_R, s)	5	5
Governor regulation (R, pu)	0.05	0.05
Damping factor (D, pu)	1	1
Inertia constant (H, s)	6.5	6.3